Accuracy of Wind Measurements Using an Airborne Doppler Lidar

JOHN J. CARROLL

Department of Land, Air and Water Resources, University of California, Davis, CA 95616

(Manuscript received 21 January 1985, in final form 15 June 1985)

ABSTRACT

Errors in airborne Doppler lidar measurements of the wind are evaluated using simulated wind fields and simulated lidar data derived from these wind fields. The primary motivation for this study is the evaluation of several sources of error in the measurement technique. Two types of errors are examined: those due to errors in aircraft velocity and those due to the displacement of the spatially varying wind field during the time between two intersecting looks at the sample volume.

It is found that small errors in the measured aircraft ground speed and track angle produce large errors in the recovered wind speed and direction. Errors in recovered wind speed and direction are strongly dependent on wind direction relative to the flight path. Errors due to nonsimultaneous samples can also be large, and are strong functions of the range to the sample volume, wind direction, wind speed, and disturbance amplitude. Recovery of accurate wind fields in such cases requires that the lidar data be displaced to account for advection so that the intersections are defined by air parcels rather than fixed points in space.

The analysis is focused on a particular type of lidar system, but in fact, the results are applicable to other remote sensing systems, such as Doppler radars, that do not utilize simultaneous sampling of the same sample volume.

1. Introduction

Detailed knowledge of the variation of the wind at space scales of a few hundred meters is needed for the full understanding of phenomena such as local severe weather. In situ instrumentation for such measurements is not practical because physical limitations preclude installation of hundreds of sensors in the appropriate place on short notice, and they preclude sampling at all heights known to be important to the problem. An alternative to in situ measurements is the use of remote sensing as with a ranging Doppler device (Jorgensen et al., 1983). One such device is an infrared laser system developed by NASA and adapted for use in a large aircraft. The system is described in Bilbro et al., (1984) and will not be extensively described here. However, the major properties of the lidar and its application will be discussed as these are very important to the work described in this paper.

The lidar consists of a continuous-wave carbon dioxide laser (wavelength = 10.6 μm), whose output is modulated to emit pulses that are transmitted in a controllable direction. The radiation backscattered by particles in the air is collected by a telescope and recombined with a small amount of radiation from the source and focused on a detector. The interference between the backscattered signal and the local signal creates a beat frequency at the detector which is equal to the Doppler shift in the returned radiation. Using appropriate timing of samples of the backscattered signal, the velocity component along the line of sight can be measured as a function of range. If a second beam crosses the first at some range, the line-of-sight speed in that direction can also be measured and the speed and direction of the flow in the plane defined by the two beams can be determined. Rather than use two lasers displaced in space with overlapping scan angles, the airborne system uses the aircraft to move a single laser which scans 20 degrees forward and aft of the normal to the flight path. The alternating lidar pointing defines a field of intersections along the flight track as shown in Fig. 1. At each of these intersections, the two line-of-sight speeds can be used to calculate the horizontal wind speed and direction—assuming the sets of scans are in the horizontal plane.

In practice the samples are not taken at a point, but over cylindrical volumes nominally 300 meters long (for a 2 microsecond pulse duration). Also, multiple (40 to 100) pulses are used with the line of sight held constant and the backscattered signals from these pulses are averaged to obtain the Doppler speed in the sample volume. The actual line-of-sight sample volume is about 300 m long, 20–300 m wide, as measured parallel to the flight path (with 150 m being typical) and a quarter of a meter thick. The intersections of the forward- and aft-looking sample volumes are diamond shaped, having dimensions of about 150 m on a side. The geometry and nomenclature are illustrated in Figs. 2 and 3. With this instrument and the sampling techniques described, it should be possible to obtain a detailed map of the horizontal wind over a large area (10 to 20 square kilometers) in only a few minutes.

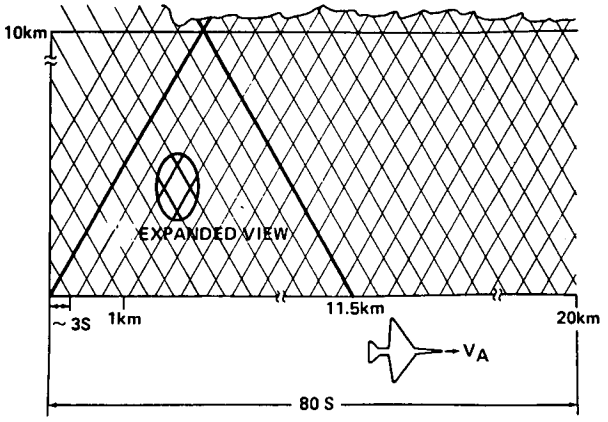

FIG. 1. Plan view of sample domain showing airborne Doppler lidar scan pattern.

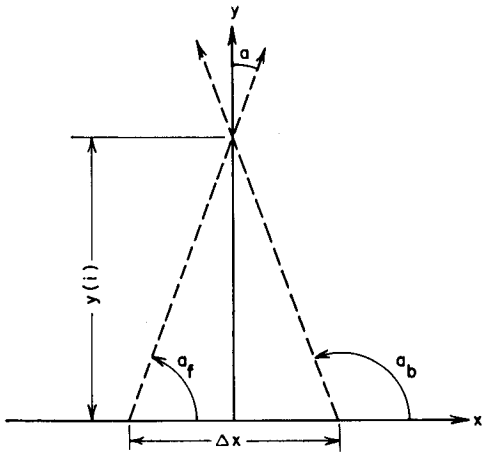

FIG. 3. Depiction of the range to the sample volume (Y), scan angle (a), and line-of-sight angles (a_f, a_b).

There are, however, several significant assumptions on which this technique depends. These include the assumptions that: (i) the beam position is exactly known, (ii) the aircraft ground speed and track angle are exactly known, and (iii) the time delay between a forward and backward look at the same point in space will not cause serious errors. Beam-pointing errors can result from inaccurate positioning of the lidar optics or from inaccurate pitch and roll information. These errors can cause the incorrect calculation of the aircraft velocity contribution to the line-of-sight speed and misinterpretation of where in space the data apply. Of these, the former is the far more serious since the aircraft speed is an order of magnitude greater than the wind speed. For the same reason, errors in the aircraft velocity relative to the ground could produce large errors in the recovered wind field. The validity of the third assumption depends on how quickly the wind changes in a given sample volume as compared to the time delay between the forward and backward samples. This report examines these sources of potentially significant errors. A discussion of other types of errors associated with Doppler techniques is presented in Doviak et al., 1976.

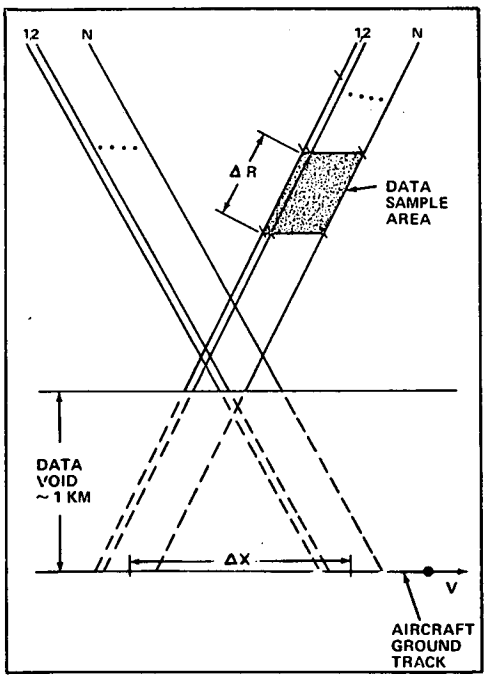

FIG. 2. Close up view of two intersecting scans showing idealized sample volume overlap area: V_a is the aircraft ground speed, ΔR the range resolution (dependent on pulse width), N is the number of pulses within a data volume and Δx is the distance the aircraft travels between the foreward and aft observations.

2. Simulations

In order to test the sensitivity of the lidar system to these sources of error, wind fields and the performance of the lidar were simulated in the following manner. A wind field was generated with known properties that could be constant or varying in space and time. Since errors in beam positioning and aircraft velocity produce similar errors in the recovered wind field, it is assumed in the first of these calculations that the lidar system is ideal and errors in the recovered winds are caused by ground speed and track angle errors. The second simulation was undertaken to study the errors caused by the time delay in sampling from two directions. There were no positioning or aircraft velocity errors, but the wind speed and direction vary sinusoidally in the horizontal plane and these waves were advected at the mean wind speed. These latter simulations were performed for different mean wind speeds, mean directions, disturbance amplitudes and aircraft speeds.

In all cases the modeled wind at the ith range bin at time t is:

$$V(i, t) = V_0 + \Delta V \sin k[Y(i) \sin D_0 - V_0 t]$$
$$D(i, t) = D_0 + \Delta D \sin k[Y(i) \sin D_0 - V_0 t] \quad (1)$$

where V_0 and D_0 are the mean wind speed and direction and ΔV and ΔD are the perturbation amplitude. These and all other symbols are defined in Appendix A. The variable Y is the range to the intersection along the normal to the flight path and is computed from:

$$Y(i) = [150 + 300(i - 1)] \cos a \quad (2)$$

where a is the angle between the normal to the flight path and the line-of-sight directions and a range resolution of 300 m is assumed.

The contribution of the wind to the forward (V_f) and backward (V_b) line-of-sight speed for the ith range bin at time t is:

$$V_f(i) = -V(i, t) \cos[a_f - D(i, t)]$$
$$V_b(i) = -V(i, t) \cos[a_b - D(i, t)] \quad (3)$$

where a_f and a_b are the fore and aft viewing angles measured counterclockwise from the positive x axis.

The effect of aircraft speed and direction errors were examined by computing the line-of-sight speeds in the forward (V_{af}) and backward directions (V_{ab}) due to the aircraft motion:

$$V_{af} = (V_a + \Delta V_a) \sin(a_f - \Delta D_a)$$
$$V_{ab} = (V_a + \Delta V_a) \sin(-a_b + \Delta D_a). \quad (4)$$

In these calculations, $\Delta V = \Delta D = 0$ in Eq. (1). All line-of-sight speeds are defined to be positive if directed inward. For simplicity the aircraft path is assumed to be along the positive x axis. The scan angle (a) is 20 degrees from the normal and ΔV_a and ΔD_a are the errors in aircraft ground speed and track. Aircraft motion along the line of sight was added to the line-of-sight wind speeds calculated using (3). The expected aircraft contribution to the "measured" line-of-sight speeds [calculated from (4) with $\Delta V_a = \Delta D_a = 0$] were then subtracted from the total line-of-sight speeds, giving values of V_f and V_b, which includes both the wind and the aircraft velocity error.

Given pairs of values for V_f and V_b, the alongtrack and crosstrack wind components can be computed from the line-of-sight components and knowledge of the line-of-sight viewing angles:

$$U_r(i) = \frac{V_b(i) - V_f(i)}{\sin\delta_b + \sin\delta_f}$$
$$V_r(i) = \frac{V_b(i) + V_f(i)}{\cos\delta_b + \cos\delta_f}. \quad (5)$$

The form of these equations follows the conventions used by NASA and assumes the scans are symmetric about the normal to the flight path. The arguments for the sine and cosine functions are defined as:

$$\delta_f = a_f + 90$$
$$\delta_b = -(a_b + 90). \quad (6)$$

These components are transformed to the vector wind speed and direction and the difference between the true wind speed and vector direction and the recovered speed and direction are the errors.

The second type of simulation differs in several ways from the aircraft error tests. Here, the time delay between looks is represented by the change in the simulated wind within each range bin due to the change in phase resulting from advection of a wave at the mean wind speed. However, since the lidar actually averages over a 300 m path length, the line-of-sight components are computed from the average wind speed and direction in the sample volume valid at the time of the sample. For the forward direction, the wind in a sample volume is given by:

$$V(i, t) = \frac{1}{n} \sum_{j=1}^{n} V_0 + \Delta V \sin k[y(j) \sin D_0 - V_0 t]$$
$$D(i, t) = \frac{1}{n} \sum_{j=1}^{n} D_0 + \Delta D \sin k[y(j) \sin D_0 - V_0 t]. \quad (7)$$

The $\sin D_0$ factor defines the lines of constant phase to be normal to the propagation direction, D_0. Here $y(j)$ is the range to the center of subvolumes within the range bin as defined by:

$$y(j) = y(i) + \left[\frac{150}{n} - 150 + \frac{300(j - i)}{n}\right] \cos a. \quad (8)$$

Similarly, the average speed and direction at the time of the backward look are:

$$V(i, t + \Delta t) = \frac{1}{n} \sum_{j=1}^{n} V_0 + \Delta V \sin k[y(j) \sin D_0 - V_0(t + \Delta t)]$$
$$D(i, t + \Delta t) = \frac{1}{n} \sum_{j=1}^{n} D_0 + \Delta D \sin k[y(j) \sin D_0 - V_0(t + \Delta t)] \quad (9)$$

where the delay time (Δt) is a function of the range and airspeed given by:

$$\Delta t = 2[150 + 300(i - 1)] \frac{\sin a}{V_a}. \quad (10)$$

In the simulations reported, the number of subvolumes used (n) per sample volume was 30. Note that the phase speeds of the wave are defined relative to the ground rather than to the aircraft since the lidar sample volumes are defined as fixed points in space and independent of the aircraft speed.

Using Eqs. 7, 9 and 10, the differences in the wind

speed and direction between the fore and aft scans of the ith range bin can be expressed as:

$$V' = \Delta V(\sin\alpha - \sin\alpha\cos\beta + \cos\alpha\sin\beta)$$
$$D' = \Delta D(\sin\alpha - \sin\alpha\cos\beta + \cos\alpha\sin\beta) \quad (11)$$

where:

$$\alpha = k[Y(i)\sin D_0 - V_0 t]$$

is the phase of each perturbation in bin i at time t and

$$\beta = k[Y(i)\sin(aV_0/V_a)]$$

is the phase shift in bin i between the fore and aft scans. Combining (11) and the second of (3) gives

$$V_b = -[V(i, t) + \Delta V(\sin\alpha - \sin\alpha\cos\beta + \cos\alpha\sin\beta)]\cos\{a_b - [D(i, t) + \Delta D(\sin\alpha - \sin\alpha\cos\beta + \cos\alpha\sin\beta)]\}. \quad (12)$$

Obviously if both ΔV and ΔD are zero, or if the time delay were zero, i.e., $\beta = -kV_0\Delta t = 0$, Eq. (12) would reduce to the second expression in Eqs. (3) and no error would occur in this simulation. Given the complexity of Eq. (12), the nonsimultaneous sampling errors were evaluated using a number of calculations with various values of the relevant parameters. In all of these simulations, the phase difference between the speed and direction perturbations is exactly zero.

In all simulations, the aircraft flight track is along the x axis, so that the aircraft heading is exactly zero and does not appear explicitly in the equations. Four wind speeds were examined, (2.5, 5, 10 and 20 m s^{-1}) and seven wind directions (0, 20, 50, 90, 130, 160 and 180 degrees as measured counterclockwise from the x-axis) were used. The wave amplitudes for the nonsimultaneous error tests were 0, 2, 4 and 8 m s^{-1} for the speed variations and 0 and 10 degrees for the direction variations. The wavelengths varied between 20 meters and 4370 meters in each case. The results of the second set of simulations are expressed either as the actual error or as the percent difference between the recovered wind field and the correct wind normalized with respect to the amplitude of the imposed disturbance. The "correct" wind speed and direction for a given range bin is the average of the values at the forward look time and the backward look time. The scaled percentual errors were computed from:

$$\sum_S(i) = \left[V_r(i) - \frac{V1(i, t) + V1(i, t + \Delta t)}{2}\right]\frac{100}{\Delta V}$$
$$\sum_D(i) = \left[D_r(i) - \frac{D1(i, t) + D1(i, t + \Delta t)}{2}\right]\frac{100}{\Delta D}. \quad (13)$$

The use of the average speed and direction over the two sample times is arbitrary. It was chosen simply to represent the same quantity that would be interpreted from the data.

3. Results

The effect of errors in aircraft velocity on the recovered wind speed and direction were calculated separately. In these calculations the true wind speed was 5.1 m s^{-1} (10 kt) from various directions relative to the flight path. True aircraft speed is 129 m s^{-1} (250 kt) with the simulated ground speed errors being 1, 2, 4, 8 and 12 knots, and ground track errors (equivalent to beam pointing errors) were 0.1, 0.4 and 0.8 degrees.

The errors in the recovered wind field caused by ground speed errors are shown in Fig. 4. Wind speed errors are similar in magnitude to the aircraft speed

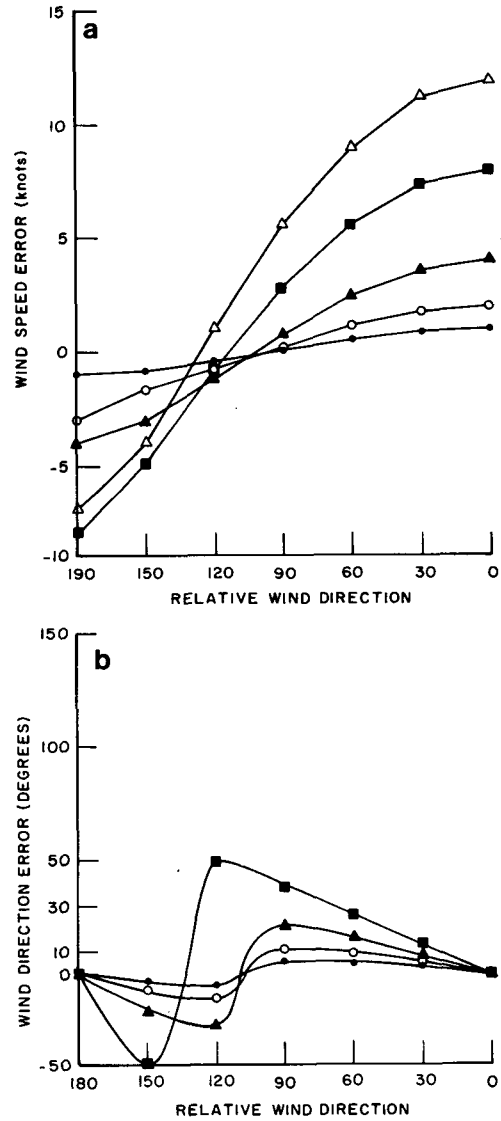

FIG. 4. (a) Wind speed errors due to aircraft ground speed errors versus wind direction relative to the flight path. Dots are for ΔV_a = 0.52 (1), circles, ΔV_a = 1.03 (2); closed triangles, ΔV_a = 2.06 (4), closed squares, ΔV_a = 4.12 (8) and open triangles, ΔV_a = 6.18 (12) m s^{-1} (kt); V_a = 129 m s^{-1} (250 kt), V_0 = 5.2 m s^{-1} (10 kt). (b) As in (a) but for wind direction errors.

errors when the wind is parallel to the flight path and are very small when the wind direction is about 120° from the flight path. Conversely, wind direction errors are very large when the wind direction is across the flight path reaching ±50° for ΔV_a = 8 kt at D_o = 120 deg.

Figure 5 illustrates the dependence of the recovered wind on ground track errors. Wind speed errors are quite large for track errors as small as 0.8 deg and are strong functions of the wind direction relative to the aircraft. Similarly, large directional errors in the recovered wind occur for all except winds nearly normal to the flight path.

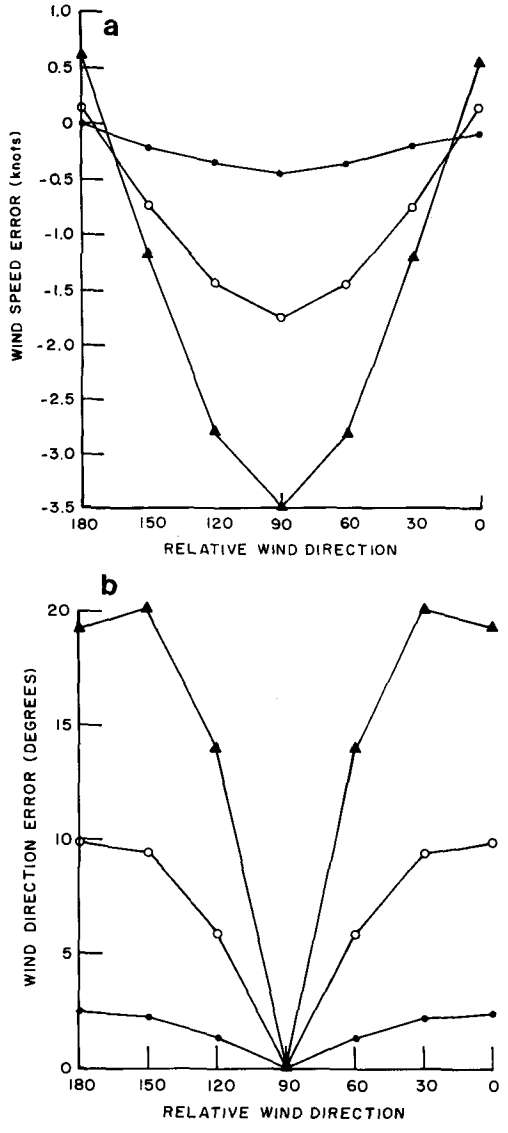

FIG. 5. (a) Effect of track angle errors on wind speed as a function of wind direction relative to the flight path. Dots are for ΔD_a = 0.10°; circles, ΔD_a = 0.4°; and closed triangles for ΔD_a = 0.8°. V_a = 129 m s^{-1} (250 kt), V_0 = 5.2 m s^{-1} (10 kt). (b) As in (a) but for wind direction.

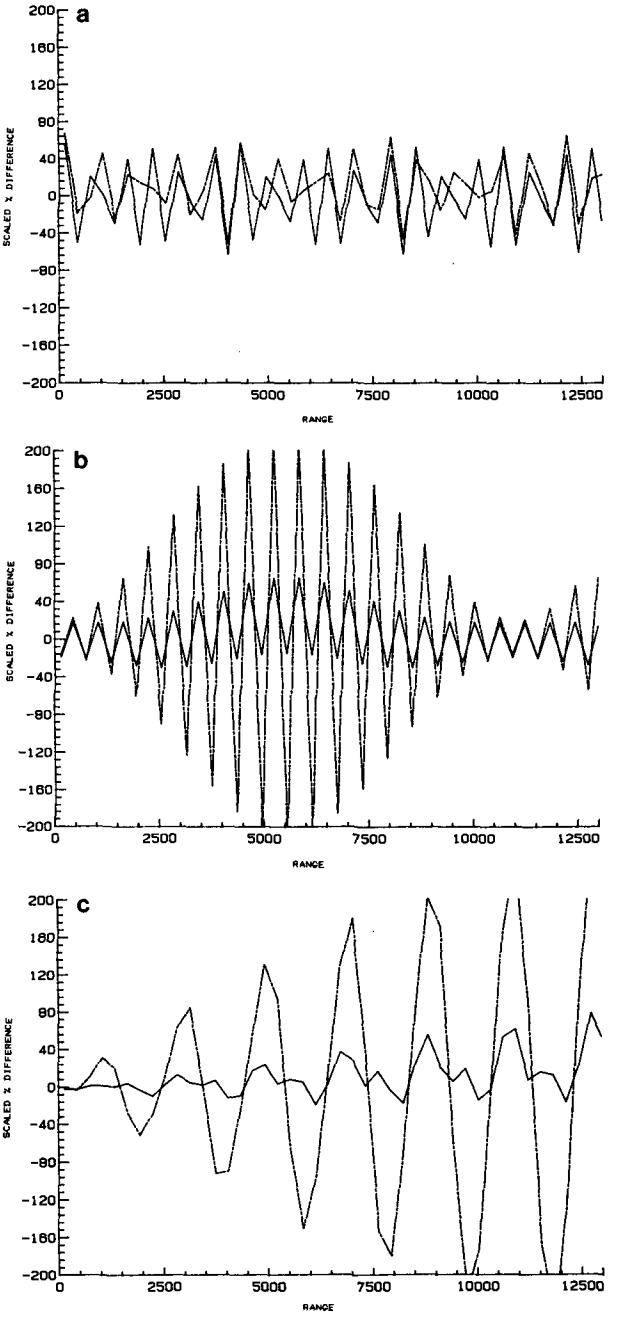

FIG. 6. (a–c) Differences between actual and recovered data as percent of perturbation amplitude in speed (solid) and direction (dot–dashed) versus range for V_0 = 10, V_a = 129 m s^{-1}, and D_0 = 90°, and for the wavelengths 210, 600 and 1920 m.

The nonsimultaneous sampling errors were evaluated for four wind speeds and seven wind directions. The amplitudes of the sinusoidal disturbances were typically 4 m s^{-1} for speed and 10 deg for the vector direction. The results of these tests are presented in several different formats.

In Fig. 6 the percent difference between the recovered wind speeds and directions and the "correct" values

are plotted as a function of range for wavelengths 210 (6a), 600 (6b) and 1920 m (6c) and for $V_0 = 10$, $V_a = 129$ m s^{-1} and $D_0 = 90$ deg. For the shorter wavelengths, $\lambda < 300$ m the effective averaging accomplished by the pulse length of 300 m causes the error to be fairly random in character and decreasing in magnitude with decreasing wavelength.

For waves longer than the sample volume, the range to the maximum (or minimum) error increases with increasing values of the phase shift parameter β and for the shorter waves may exceed 360 deg as in Fig. 6b. This appears to be true for $300 < \lambda < R/10$, where R is the maximum range. As λ approaches infinity ($k \rightarrow 0$), $\beta \rightarrow 0$, and the nonsimultaneous sampling error also approaches zero.

In Fig. 7 the scaled percent rms errors averaged over all 45 range bins are shown as isopleths in a space defined by the wind direction and disturbance wavelength. For these plots, the perturbation amplitudes are 4 m s^{-1} in speed and 10 deg in direction. The patterns depicted are similar to those at other wind speeds and perturbation amplitudes.

The speed errors averaged over all range bins vary considerably with wavelength, wind direction, and wind speed. The scaled maximum speed errors occur for directions near 45 deg and for wavelengths between 0.7 and 8 times the sample volume length. The extreme values among range bins do not exceed three times the rms error computed over all range bins. The distribution of the error with direction shows a minimum near 120 degrees.

The directional errors (7b) are large for wind directions between 40 and 120 deg and for wavelengths between 0.7 and about 10 times the sample volume length, with a maximum for $D_0 \approx 60$ deg and $\lambda \approx 3$ times the sample length. Unlike the speed errors, the maximum error in direction decreases with increasing wind speed.

The effect of wind speed and direction on the error distribution is depicted in Fig. 8. The isopleths are the scaled percentual rms errors averaged over range and wavelength. As one would expect, the scaled speed errors generally increase with wind speed (8a). However the directional errors decrease with increasing V_0 (8b) since for the same perturbation amplitude, as the total speed increases, the directional error decreases. Conversely at low wind speeds, the sensitivity of the direction calculation to the fixed amplitude errors in the component wind speeds increases. For the case shown, the speed perturbation amplitude is 4 m s^{-1}. Therefore, for $V_0 < 4$ m s^{-1}, the simulated flow is undergoing flow reversals with time which result in large directional errors at low mean speeds.

To further illustrate these dependencies, the unscaled rms errors were averaged over range, direction and wavelengths and plotted against wind speed in Fig. 9. Two regimes are apparent: for $\Delta V/V_0 > 1$, the errors increase with decreasing V_0, i.e., when the perturbation amplitudes exceed the mean flow then flow reversals can occur and the recovered wind field errors will be large. For $\Delta V/V_0 < 1$, the average errors increase essentially linearly with V_0. The similarly averaged directional errors are shown in Fig. 9b. These show the same trends as in Fig. 8b, the wind directions become increasingly indeterminate as the mean wind speeds approach zero. The results illustrated in Fig. 9 also show that the magnitude of the errors is not linearly proportional to the perturbation amplitudes—a result also to be expected given the form of Eq. 12.

One result that seems contrary to intuitive expectations is the lack of symmetry about $D_0 = 90$ deg. As illustrated in Fig. 10, this asymmetry is the result of the interaction of the speed and direction perturbations. Clearly if $\Delta V = 0$ the speed errors (10a) are symmetric about 90 and if $\Delta D = 0$ the directional errors (10b) are symmetric about $D_0 = 90$ deg. The errors in the nonzero amplitude variable vary sinusoidally through one full cycle between $D_0 = 0$ and 180 deg.

These calculations were all performed with zero phase difference between the speed and direction perturbations. Introducing a phase shift will change the distribution of errors with D_0 and range but will not

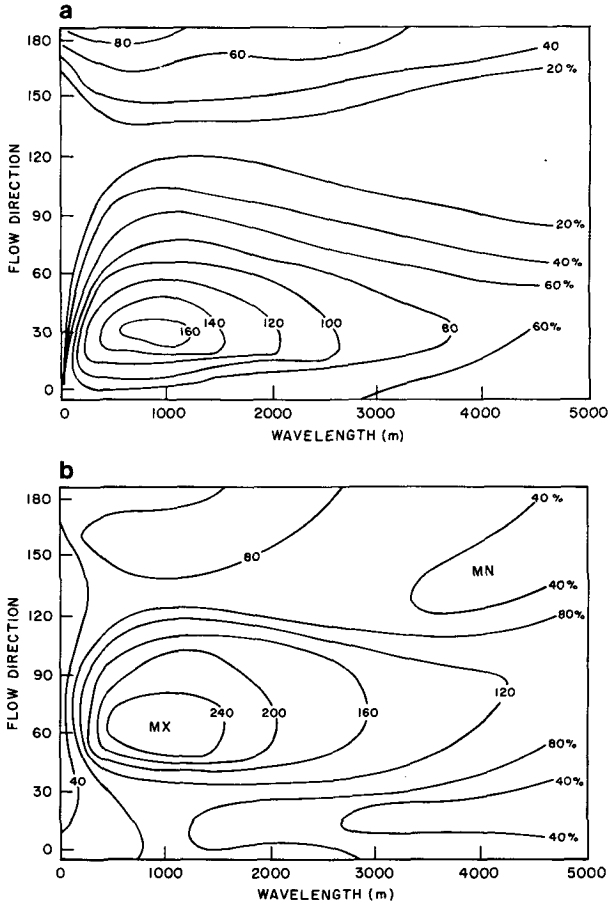

FIG. 7. Scaled rms errors (%) in speed (a) and direction (b) as a function of wavelength and wind direction for $V_a = 129$, $V_0 = 10$ and $\Delta V = 4$ m s^{-1} and for $\Delta D = 10°$.

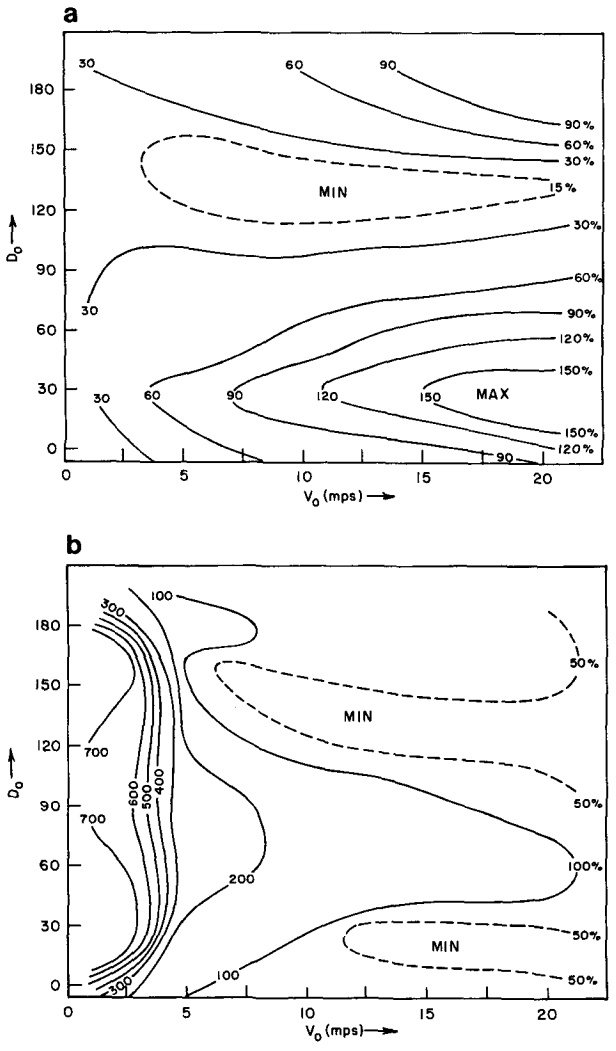

FIG. 8. Scaled rms errors (%) in speed (a) and direction (b) averaged over wavelength as a function of wind speed and direction for V_a = 129 and ΔV = 4 m s^{-1} and for ΔD = 10°.

change the maximum magnitude of the errors greatly. For example, introduction of a 45 deg phase lead in the direction perturbations results in a slight reduction in the errors for $20 < D_0 < 160$ deg and a 50% increase at D_0 = 0 and 180 deg (V_0 = 20), i.e., the wind direction of the maximum error shifts from D_0 = 45 to D_0 = 0 and 180 deg.

The effect of varying the aircraft speed was investigated. The nonsimultaneous sampling errors in both speed and direction decreases with increasing V_a. The dependence is not simply proportional to $1/V_a$ since the ground speed enters the problem through the parameter $\sin(aV_0/V_a)$.

4. Summary and conclusions

Given the fact that aircraft speed is an order of magnitude greater than typical wind speeds, errors in the recorded angle between the beam direction and the aircraft flight direction will produce an error in the line-of-sight wind component of the same order of magnitude of the wind component. Therefore it is essential that beam position relative to the flight path be known to a very high degree of accuracy for each shot. If the recovered wind field (assuming perfect performance by the rest of the system) is to be within 5° of the correct direction and 10% of the correct speed, this angle must be known to within 0.2°. For similar reliability in the results, the aircraft ground speed must be known to within 1 knot. Such tolerances are difficult to attain using the aircraft navigation system. However, by including forward and aft downslanted lidar views of the ground in the scan sequence, the aircraft velocity can be measured directly.

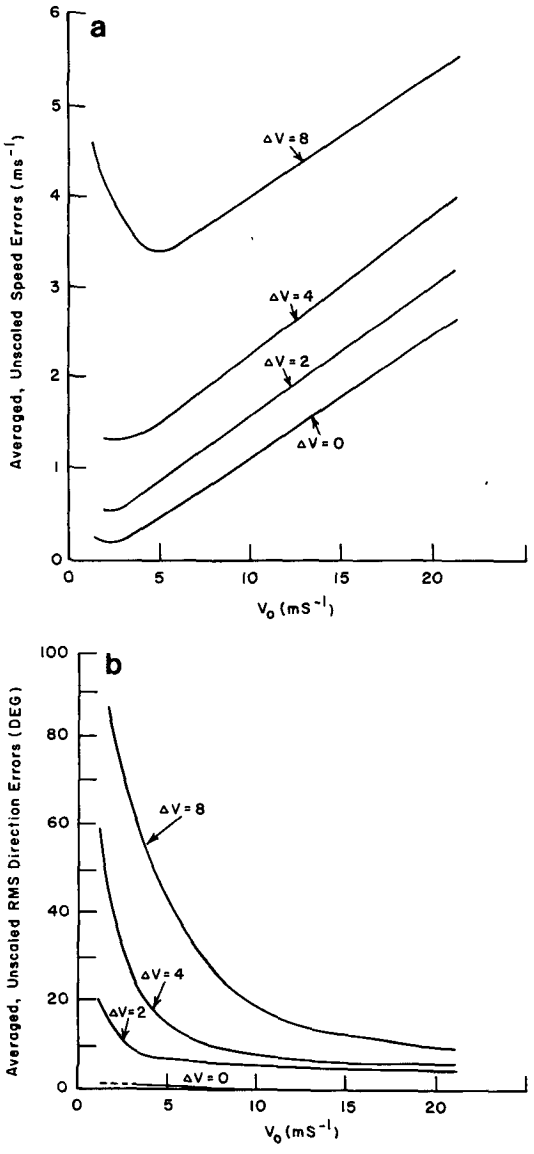

FIG. 9. Unscaled rms errors in speed (a) and direction (b) averaged over wavelength versus wind speed (V_0) for various speed perturbation amplitudes and for ΔD = 10° and V_a = 129 m s^{-1}.

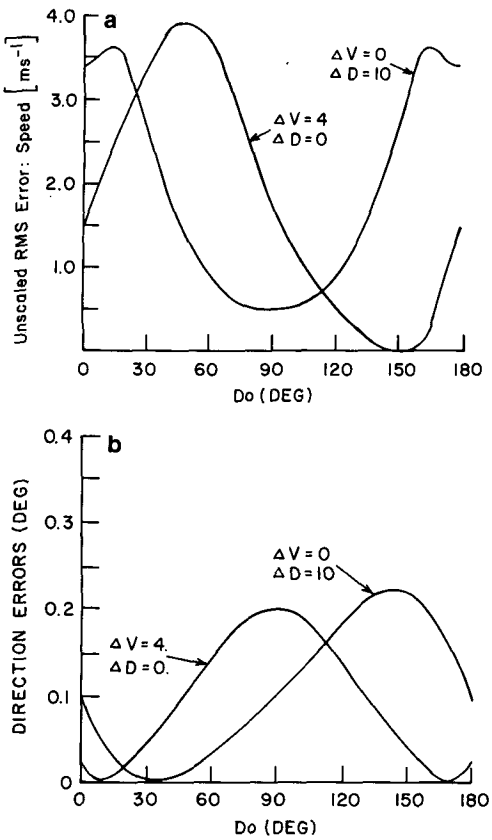

FIG. 10. Unscaled rms errors in speed (a) and direction (b) versus wind direction averaged over wavelength for $\Delta V = 4$ m s^{-1}, $\Delta D = 0°$ and $\Delta V = 0$, $\Delta D = 10°$ and for $V_0 = 20$ and $V_a = 129$ m s^{-1}.

The nonsimultaneous sampling errors can also be large. The maximum rms errors averaged over all range bins are found for $200 < \lambda < 2000$ meters, but are distributed asymmetrically with wind direction if both speed and directional perturbations are present. The scaled rms speed errors increase in magnitude at all D_0 with increasing V_0, ΔV and ΔD. Speed and direction errors decrease with increasing V_a. Directional errors increase with increasing ΔV and ΔD but decrease with increasing V_0—especially for $\Delta V/V_0 > 1$.

Speed and direction nonsimultaneous sampling errors vary considerably with range. For wavelengths smaller than the sample volume, the error magnitudes are distributed equally with range. For wavelengths larger than 300 m but less than the maximum range, the maximum errors occur at a range that increases with increasing wavelength. For long waves, the error amplitude increases monotonically within the calculational domain. The maximum absolute value for any range bin does not exceed three times the rms value calculated over all range bins.

The systematic errors associated with the time delay in the sampling technique should be correctable or at least can be estimated directly from the lidar data. By computing the spectral distribution of the variance in the line-of-sight speed data, the wavelengths and amplitudes of the disturbances in the wind field can be estimated along each look angle. From these the actual wavenumber spectrum can be estimated and the approximate error magnitude estimated from the results given here. If the estimated errors are significant, an advection correction can be made to reduce this error. In principle, the aircraft motion integrates the spacial variations of the wind and the averaged aircraft derived wind field can be used as a first estimate of the mean wind in the sampling domain. This of course presumes that the aircraft motion is well documented. The first set of samples can be advected, using this averaged wind and the range dependent time delay, to a location representing the same parcel of air and the intersections defined accordingly. The presumption is that eddies do not change their kinematic properties quickly during the delay (Taylor's frozen turbulence hypothesis) and that translation of all eddies is by the mean wind. Once the pairs of forward and backward samples are so determined, a wind field can be determined for the sampled domain. This new estimate could then be used to refine the first estimate of the mean wind and the advection adjustment recomputed. This iterative procedure could be repeated (or modified to allow for large-scale gradients in the wind) until the differences in wind fields between estimates are acceptably small.

Equally important, but not always practical, would be to fly the aircraft such that the vector wind direction is 110 to 150° aft of the aircraft heading.

A high confidence in the representativeness of the recovered wind field can be assigned if:

1) The recovered wind field is very smooth;
2) the recovered wind field shows spacial variability at large scales ($\lambda \gg R$) with light to moderate wind speeds ($V_0 < 5$ m s^{-1});
3) Whenever the mean winds are very light ($V_0 < 2.0$ m s^{-1}) and the fields are fairly smooth.

Recovered wind fields that show a great deal of structure at moderate space scales imply that the real flow has significant amplitude speed and direction variations, but the depicted structures in the recovered wind field cannot be interpreted as the real wind structure.

A word of caution is in order. The error evaluations due to the time delay between sampling of a given sample volume were obtained from a model in which constant amplitude waves are advected by a mean wind. The real atmosphere is not so constrained. In reality, real disturbances are not constant amplitude, can be the result of simultaneous interaction of multiple scales and advection of the smaller scale perturbations are in part due to advection by the larger scales as well as by the mean wind. In the simulation model, the errors would go to zero if $V_0 = 0$. In the real atmosphere, local accelerations can occur in the absence of

a mean wind due to buoyant forces as in a freely convecting atmospheric boundary layer. Therefore these results should not be extended beyond their inherent limitations and should be viewed as an indication of the kinds of uncertainty one will encounter in the use of this type of sampling.

Acknowledgments. Support for this work was provided by the California Agricultural Experiment Station and by NASA through contract NAS8-34730.

APPENDIX A

Nomenclature

a	magnitude of the line-of-sight angle measured from the normal to the flight path
a_f, a_b	forward, backward line-of-sight direction (positive outward) measured from the positive x axis
D_0	base state wind direction, measured counter clockwise from x axis
$D(i, t)$	actual wind direction in the ith sample volume at time t
ΔD	amplitude of the sinusoidal perturbation superimposed on D_0
ΔD_a	error in the aircraft track angle
k	wave number of the perturbation $= \frac{2\pi}{\lambda}$
N	number of laser pulses in a constant line-of-sight averaged to define the Doppler speed in each range bin
n	number of subvolume elements used to average the Doppler velocity in each range bin
R	distance to last range bin
V_0	base state wind speed
V_a	aircraft air speed
ΔV	amplitude of the perturbation imposed on the wind speed
ΔV_a	error in aircraft ground speed
$V(i, t)$	actual wind speed in the ith range bin at time t
V_b, V_f	Doppler line-of-sight speeds (positive inward) for the backward and forward looks
V_{ab}, V_{af}	aircraft velocity contribution to the backward and forward line-of-sight speeds
δ_b, δ_f	complements of the line-of-sight directions (cf. Eq. 5)
α	phase of perturbation in bin i at time t
β	phase shift in bin i between t and $t + \Delta t$
λ	wavelength of the imposed perturbation (m).

REFERENCES

Bilbro, J., G. Fichtl, D. Fitzjarrald, M. Krause and R. Lee, 1984: Airborne Doppler wind measurements. *Bull. Amer. Meter. Soc.*, **65**, 348–359.

Doviak, R. J., P. S. Ray, R. G. Strauch and L. J. Miller, 1976: Error estimation in wind fields derived from dual Doppler radar measurement. *J. Appl. Meteor.*, **15**, 868–878.

Jorgensen, D. P., P. H. Hildebrand and C. L. Frush, 1983: Feasibility test of an airborne pulse—Doppler meteorological radar. *J. Climate Appl. Meteor.*, **22**, 744–757.